NORSAR

ROYAL NORWEGIAN COUNCIL FOR SCIENTIFIC AND INDUSTRIAL RESEARCH

Scientific Report No. 2-79/80

SEMIANNUAL TECHNICAL SUMMARY 1 October 1979—31 March 1980

By
A. Kr. Nilsen (ed.)

Kjeller, June 1980

VI.4 Mapping of Upper Mantle Heterogeneities

The method developed by Aki, Christoffersson and Husebye (1977) - denoted the ACH method in the following - for 3-dimensional inversion of P-wave residuals from a 2-dimensional network of stations has been successfully applied in studies of crustal and upper mantle heterogeneities in various parts of the world. The network data used have mainly been extracted from local networks and thus not generally available. The only exception in this regard is the ISC bulletins containing P-residuals for all those stations regularly reporting to ISC. In certain regions like Central Europe the distribution of ISC-reporting stations is sufficiently dense so as to motivate an adaption of the ACH method for analysis of this kind of data. Such an experiment is to be described in this section.

Method of analysis

The method used for analysis of P residuals from subset of ISC-reporting stations is essentially an adaptation of the ACH method to arrays of continental dimensions. A brief description of this modified inversion approach is given in the following.

The travel time residuals are related to velocity anomalies via the integral:

$$\delta T_i = \int_{A_i}^{B_i} \delta s \, d\ell \qquad \text{(VI.4.1)}$$

over the ray path in the original medium or initial earth model. Fermat's principle of least time shows that changes in the ray path caused by changes in velocity (ds) will be of second order and thus small.

The input data for each event are the focal parameters (except origin time) and a series of J-B time residuals for those stations in the network reporting the event in question. Ray parameters and azimuth (p_o and z_o) are computed from the event location to a reference station near the network center, while p and z for other receivers are estimated by the linear formulae:

$$p = p_o + \frac{\partial p}{\partial \Delta}\,\delta\Delta \qquad \text{with} \qquad \delta\Delta = -D\cos(z_o-\theta)$$

and

$$z = z_o - \frac{D\sin(z-z_o)}{\Delta}$$

where Δ is the distance from event to center station and D,θ are the relative distance and azimuth to another station within the network. Knowing p and z the ray paths are traced through the spherically symmetric starting model using an appropriate upper mantle velocity distribution. The velocity structure was represented by a smooth cubic interpolation between slowness values on a three-dimensional grid of 'knots', which in turn requires that the first and second slowness derivatives be known.

To obtain a linear relationship between observed time residuals and the velocity structure formalism above (Smith et al, 1979), we proceeded in the following manner. Let $\{f_i\}$, $\{f_i'\}$ be the values of a function f(x) and its derivative on a grid of points (i=1,2...N) with equal spacing Δx. A Hermite interpolation can be written as:

$$f(x) = \sum_{i=1}^{N} f_i H(dx^{-1}x-i) + f_i'\,\Delta x H'(dx^{-1}-i) \qquad \text{(VI.4.2)}$$

where

$$H(x) = \begin{cases} (x+1)^2(1-2x) & -1\le x\le 0 \\ 2x^3-3x^2+1 & \text{for} \quad 0\le x\le 1 \\ 0 & \text{otherwise} \end{cases}$$

$$H'(x) = \begin{cases} x(1+x)^2 & -1\le x\le 0 \\ x(1-x)^2 & \text{for} \quad 0\le x\le 1 \\ 0 & \text{otherwise} \end{cases}$$

The cubic functions have the property that they and their derivatives vanish at all points except the ith, where $H_i(x)$ is unity and its derivative is zero, and $H_i'(x)$ is zero and its derivative is unity. We do not know the $\{f_i'\}$ and so they must be estimated. Invoking continuity of second derivatives

of f(x) gives the usual spline representation where the $\{f_i'\}$ are all related to all the $\{f_i\}$. This non-local representation was rated too expensive to compute and was replaced by an estimate of $\{f_i'\}$ in which they are related only to f_{i-2}, f_{i-1}, f_i and f_{i+1} through the equation:

$$f' = G\, f \qquad \text{(VI.4.3)}$$

where

$$G = \begin{pmatrix} -2 & 1 & 2 & -1 \\ -1 & 0 & 1 & 0 \\ 0 & -1 & 0 & 1 \\ 1 & -2 & -1 & 2 \end{pmatrix}$$

Now equation (xx.2) can be written:

$$f(x) = \sum_{i}^{N} f_i\, C_i(x) \qquad \text{(VI.4.4)}$$

where

$$C_i(x) = H(dx^{-1}x-i) + \sum_{j=0}^{3} G_{ji}\, dx\, H'(dx^{-1}x-j)$$

In practice $C_o(x)$ is computed for 300 values in the range (0,1) and these are stored. The values of the $\{C_i(x)\}$ can then be 'looked up' in this table with considerable savings in computer time.

The generalization to three dimensions is obvious, namely:

$$ds(x,y,z) = \sum_{i,j,k} ds_{ijk}\, C_k(x)\, C_j(y)\, C_k(z) \qquad \text{(VI.4.5)}$$

First and second derivatives are computed by storing the corresponding derivatives of $C_o(x)$, as in the one-dimensional case.

Substituting equation (VI.4.5) into the travel time integral (VI.4.1) gives:

$$\delta T_i = s_{pqr} \int_{B_i}^{A_i} C_p(x)\, C_q(y)\, C_r(z)\, d\ell \qquad \text{(VI.4.6)}$$

The integral in eq. (xx.6) is calculated by the trapezoidal rule from known points along the ray path.

Eq. (VI.4.6) is in the form of a standard linear inverse problem for s_{pqr} and the method of solution by least squares follows that of Aki et al (1977) except on two major points. Firstly, because p and z vary slightly across the array, the assumption that the average velocity on any horizontal surface will be completely undetermined is only approximately valid. The second difference lies in the spectrum of the normal equations matrix which in turn made the stochastic inverse type of solution the obvious choice. For further details on this method and comutational schemes for associated parameters like resolution, standard errors and variance improvements, reference is made to Hovland et al (1980).

Choice of network and data used in analysis

The Central Europe seismograph network (see Fig. VI.4.1) appeared to be an appropriate one for testing the inversion scheme outlined in the previous section. The data used were, as mentioned above, P-time residuals for teleseismic events as listed in the ISC-bulletins for 1971-1974. The following station and event screening procedures were used; stations with poor detectability (Ringdal et al, 1977) were excluded as such stations appear to report systematically too late arrival times and besides they have very few observations. As regards events to be used, they were initially grouped in 10 deg azimuth/distance areas, out of which the one or two best in the sense of many and consistent observations were selected. The above screening procedure left us with 167 events out of an initial total of 1314. The final number of observations was 5807. The data base epicenters are plotted on an azimuthal equi-distant projection, centered on station BSF, in Fig. VI.4.2.

Results

The region covered by the network of stations is from 41.5°N to 54.5°N and from 4.5°W to 18.5°E, a square of side approximately 1400 km. The network data are expected to be sensitive to anomalies down to depths

comparable with the radius of its aperture. The thickness of the anomalous zone was set at 600 km, which conveniently includes the whole of the upper mantle. The grid acopted had 4 (in depth) x7x7 knots. Each interpolation coefficient affects to some extent the slowness at all depths and to a horizontal distance of 4 times the knot spacing. The slowness in the depth range 0-100 km is dominated by the values at the top level of knots, for 100-300 km the second level, 300-500 km the third level and 500-600 km by the bottom level.

The choice of the smoothing parameter θ^2 in the stochastic inverse solution is always subjective to some extent. If θ^2 is too small, the derived model will exhibit large anomalies that fluctuate rapidly between adjacent knots. Increasing θ^2 reduces the RMS of the slowness perturbations versus the reduction in RMS travel time residual for various choices of the smoothing parameter gives a trade-off curve from which one can decide at what point a decrease of θ^2 will drastically alter the model without improving the fit. Such a curve, based on the data discussed here, is displayed in Fig. VI.4.3. The overall reduction in residuals achieved by our model (Fig. VI.4.5) is 11%, from an RMS of 0.72 s for the raw data to 0.64 s. This is less than for NORSAR, which is closer to a 60% reduction. The total time variance reductions are respectively around 20% and 70%. The difference reflects a difference in the quality of the data and the larger area and correspondingly coarser grid in the Central European inversion. However, the RMS residual explained by the laterally varying models is the same for NORSAR as for the present model and is about 0.2 s.

In Figs. VI.4.4 and VI.4.5 the estimated resolution and standard errors for the velocity perturbations associated with the knots of all 4 levels are displayed. In the following detailed comments upon observed anomalous velocity features will be presented.

Level 1 (Fig. VI.4.5a) is representative of the uppermost 100 km and corresponds roughly to the lithosphere. The low velocity in the southern North Sea appears to be a real phenomenon required by the observations. However, its apparent extension northeastwards is poorly resolved by

data and thus should be given very little weight. There is a broad area of high velocity centered over Eastern Germany and comprising the Bohemian Massif and the eastern part of the Ardennes. The whole of the Paris Basin is low velocity while another high velocity region stretches from the Armorican Massif in Brittany to the Central Massif in Southern France. The Po Plain-N. Adriatic Sea exhibit a marked velocity high, but the area is poorly resolved which may reflect a lack of stations in Switzerland and N. Italy. Finally, other interesting though poorly resolved areas are the Pannonian Basin in the east and parts of the Pyrenees in the west.

Levels 2 and 3 show features that are broadly similar to each other (Figs. VI.4.5b&c), though the anomalies are somewhat smaller than for levels 1 or 4. Resolution is good except near the corners of the region, and the standard error estimates are again about 1%, larger near the edges. In level 2 the dominant feature is a velocity high covering the Paris Basin and SE-France and a velocity low over most of the German-Polish Depression. As before, parts of the Pannonian Basin and (eastern) Pyrenees remain low, while the N. Adriatic Sea now is definitely high. The Paris Basin high of level 2 becomes more dominant in level 3, encompassing also the Alps, Pannonian Basin, Po Plain and the Appennines. Further north the German-Polish depression area of velocity low appears to have been shifted slightly westward. Also Brittany and adjacent areas remain mostly low and the same applies to the eastern Pyrennees.

The anomalies in level 4 (Fig. VI.4.5.d) are with few exceptions well resolved because there are many intersecting ray paths contributing to the values at most of the knots. The picture is very different from that in the shallower levels with pronounced highs in the German-Polish Depression, Sudetes and Southern France, and similar pronounced lows in the Paris Basin and Appeninnes-Sardinia area.

Interpretation

Three possible influences on the P wave velocity will be discussed: temperature, differences in composition of the underlying mantle and sedimentary thickness at the surface.

Level 1

The velocity anomaly map for the uppermost 100 km (Fig. VI.xx.5a) shows a remarkabel correlation with both available heat flow data and the tectonic features of Central Europe. The most prominent feature is the large high in northern Germany and Poland. This region coincides with low heat flow and the Bohemian Massif and the Ardennes which are Hercynian folded units.

Consider first the effect of thermal anomalies. The heat flow in this region is on average 60 $mW \cdot m^{-2}$ with a low of 40 $mW \cdot m^{-2}$. Taking the thermal conductivity of igneous rocks to be 2.5 $W \cdot m^{-1} K^{-1}$ gives a geotherm of 24 $K \cdot km^{-1}$ for the average figure. 70 $mW \cdot m^{-2}$ gives a geotherm of 28 $K \cdot km^{-1}$. Assuming the geotherm to be constant for the whole of the 100 km thick lithosphere gives average temperature differences of 200 K for each 10 $mW \cdot m^{-2}$ change in heat flux. A typical estimate for the change of P velocity with temperature is:

$$\frac{\partial v_p}{\partial T} = -5.0\ 10^{-4}\ km \cdot s^{-1} K^{-1}$$

(Christensen 1979) giving a lateral change in v_p of 0.1 $km \cdot s^{-1}$ for 200 K or 1.2% fast for each 10 $mW \cdot s^{-2}$ low in the heat flux. The observed velocity anomalies of 2-5% fast can therefore, by this rough calculation, be explained by thermal anomalies going down to 100 km which cause the variations in heat flow from 40 $mW \cdot m^{-2}$ to 70 $mW \cdot m^{-2}$.

Another possible explanation for high velocity anomalies is that the rocks comprising the mentioned massifs have a higher velocity than elsewhere. An anomaly of 5% over 100 km produces a travel time anomaly of half a second. However, the Hercynian granites are probably only a few km thick and thus cannot account for such a large travel time residual. Between the two major high areas (see Fig. VI.4.5a) is a low velocity region over the Paris Basin and southern North Sea. The correlation with heat flow is good. There are very few stations in the Paris Basin and so it is unlikely that the time delays are caused by the sediments, which are several kilometers thick in places, because no ray paths pass through them. The sharp low in the southern North Sea also coincides with high heat flow and besides the south end of the Central Graben. The low

velocity associated with the Paris Basin may indicate a southward extension of this thermal anomaly. We mention in passing that there is low velocity over the German-Polish Depression, where there are also thick sediments and high heat flow, but these anomalies are not well resolved.

Levels 2 and 3

The anomalies in these two levels are very similar to each other and are smaller than those in level 1, and also than those in level 4 deeper down (see below). This finding agrees with the general view that the material below the lithosphere lid is more homogeneous because of its lower strength. The broad high ridge trending NW-SE across the continent cannot be explained in terms of known thermal or compositional anomalies and is plausibly accounted for by variations in the depth to the phase change at about 400 km. This phase change gives rise to a P wave velocity increase of about 5% from 8.7 to 9.2 $km \cdot s^{-1}$. For a velocity anomaly Δv in a layer of thickness x, a change in depth of the phase boundary d is given approximately by:

$$\frac{d}{x} = \frac{\Delta v}{\delta v}$$

where δv is the velocity change associated with the phase change. For level 3, $\frac{\Delta v}{v}$ = 2% and x = 200 km leading to a depth change of 80 km. For anomalies throughout level 2 and 3 of about 1% give the same result. The anomalies are therefore consistent with a shallow ridge of the olivine-spinel phase transition running NW-SE across France.

Level 4

The anomalies in level 4 are different from those in 2 and 3 and are larger. The resolution is good, and the anomalies may be related to variations in the depth of the 650 km discontinuity, where the P wave velocity increases by 10% from 10.2 to 11.2 $km \cdot s^{-1}$. For 3% anomalies in a 100 km thick layer this give a depth variation of 30 km or so for the phase boundary.

Final remarks

We have shown that it is possible to use ISC-reported travel times to obtain meaningful models of lateral variations in P wave velocity in the mantle beneath Europe. In particular, the correlation between the obtained P wave velocity anomalies exhibit a remarkably good correlation with dominant tectonic features and heat flow data. Also, the detectability estimates of Ringdal et al (1977) for Central European stations also reflect roughly the same features, and the same is likely to apply to surface wave propagation efficiency.

Studies similar to that described above are now in progress for south-east Europe and parts of Central Asia.

J. Hovland
D. Gubbins (Univ. of Cambridge, U.K.)
E.S. Husebye

References

Aki, K., A. Christoffersson and E.S. Husebye (1977): Determination of the three-dimensional seismic structure of the lithosphere, J. Geophys. Res., 82, 277-296.

Christensen, N.I. (1979): Compressional wave velocities in rocks at high temperatures and pressures, critical thermal gradients, and crustal low velocity zones, J. Geophys. Res., 84, No. B12.

Hovland, J., D. Gubbins and E.S. Husebye (1980): Upper mantle heterogeneities beneath Central Europe, Geophys. J.R. Astr. Soc., in press.

Ringdal, F., E.S. Husebye and J. Fyen (1977): Earthquake detectability estimates for 478 globally distributed seismograph stations, Phys. Earth Planet. Inter., 15, P24-P32.

Smith, M.L., B.R. Julian, E.R. Engdahl, D. Gubbins and R. Cross (1979): Linearised inversion of travel times for three dimensional earth structure, Abstract EOS Trans. Am. Geophys. Union, 59, 12.

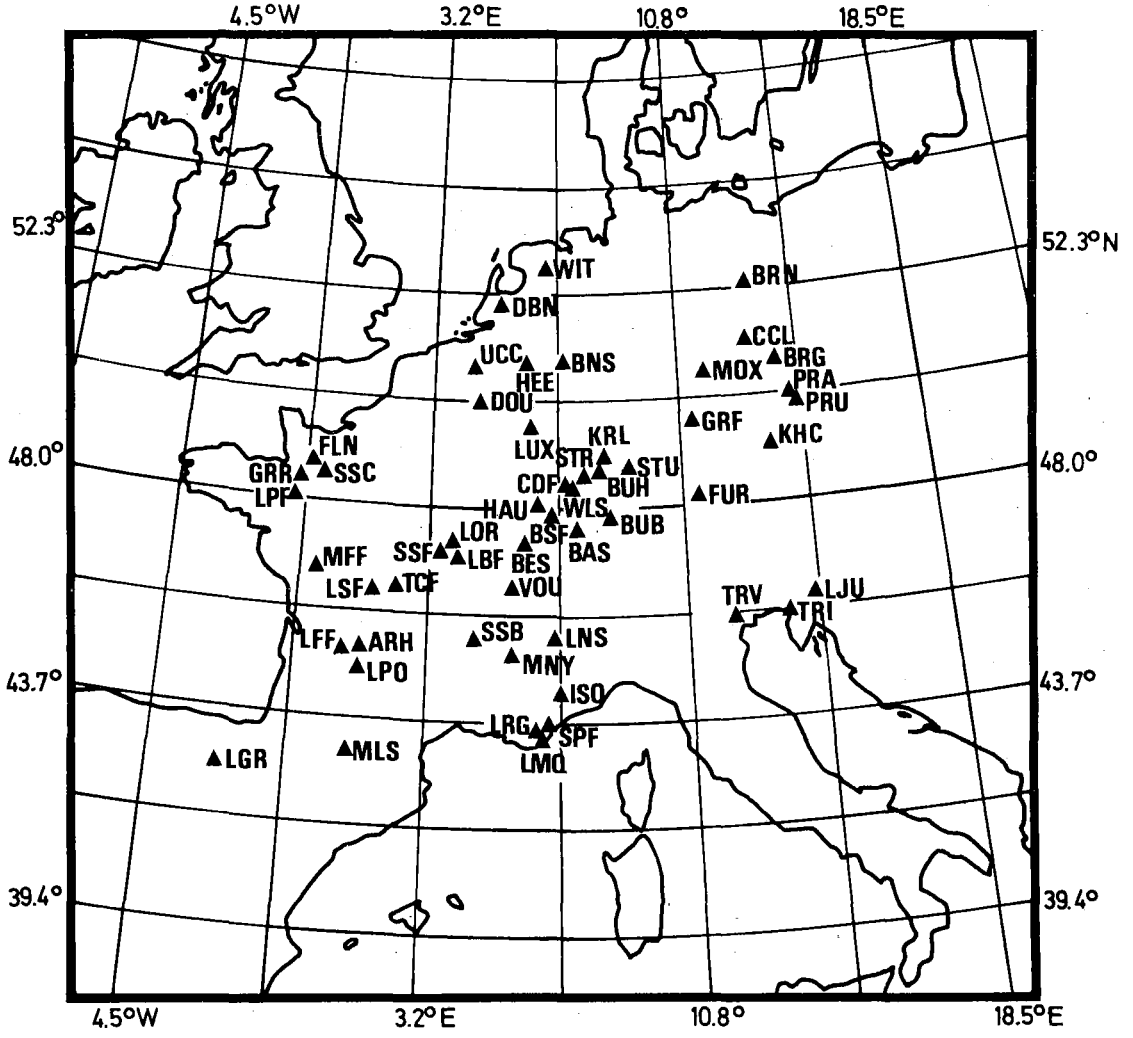

Fig. VI.4.1 Central European seismograph station network used in analysis. The intersections of the latitude/longitude grid system correspond to the nodes in the time residual inversion described in the text.

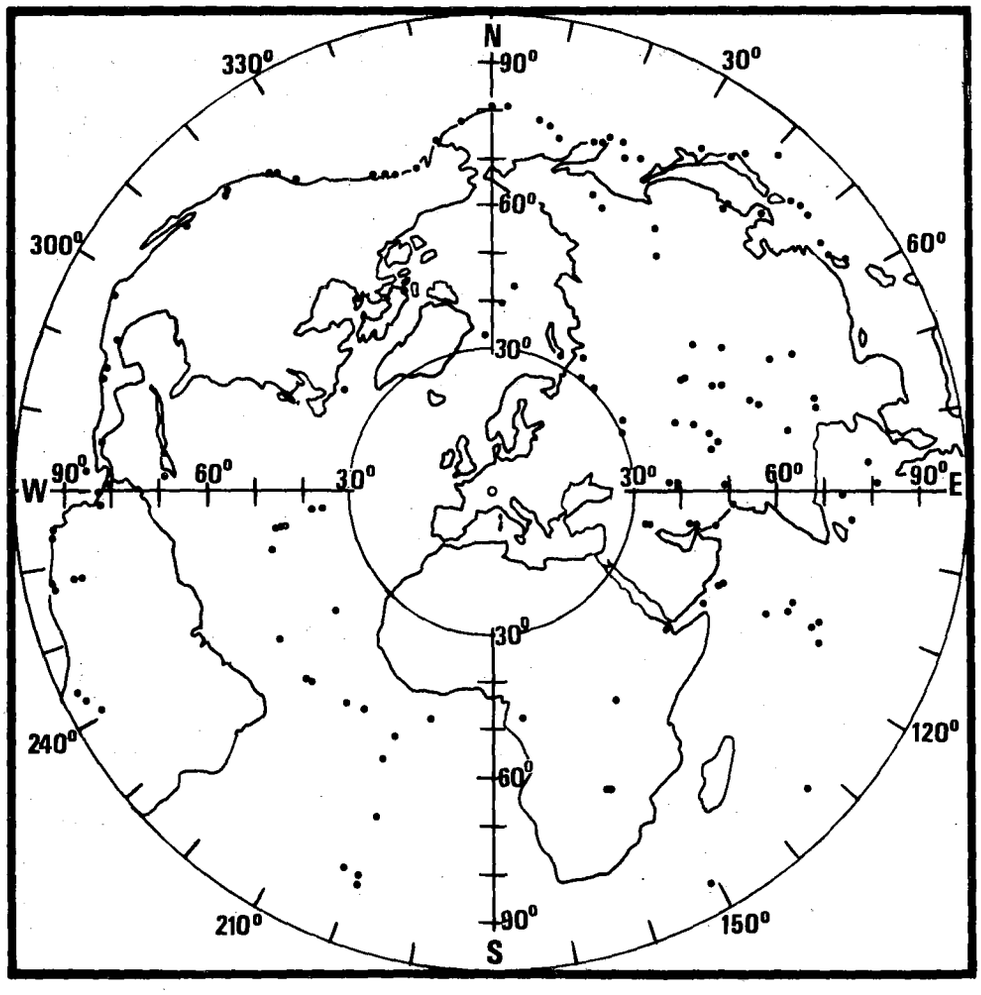

Fig. VI.4.2 Epicenter map of the 167 events used in analysis.

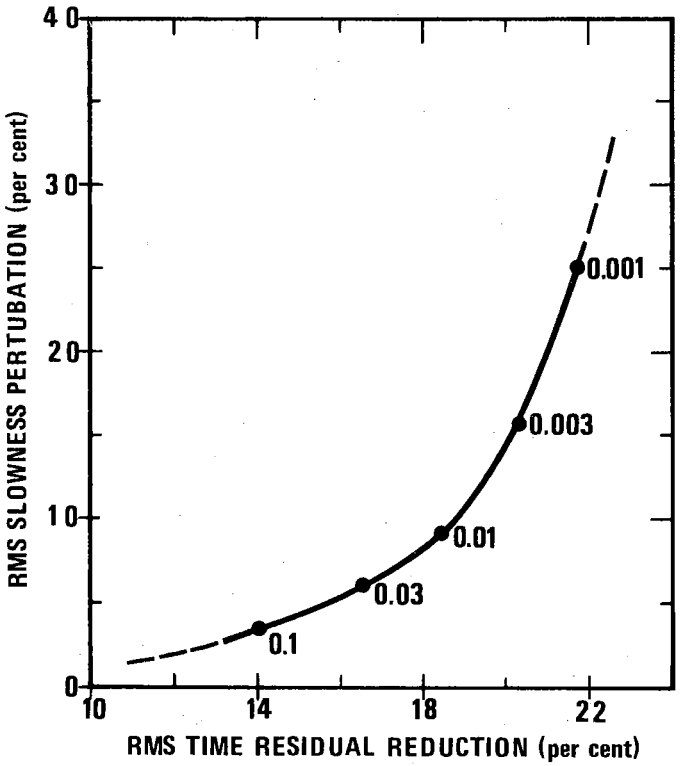

Fig. VI.4.3 RMS slowness (velocity) perturbation versus RMS time residual reduction for various values of the smoothing parameter.

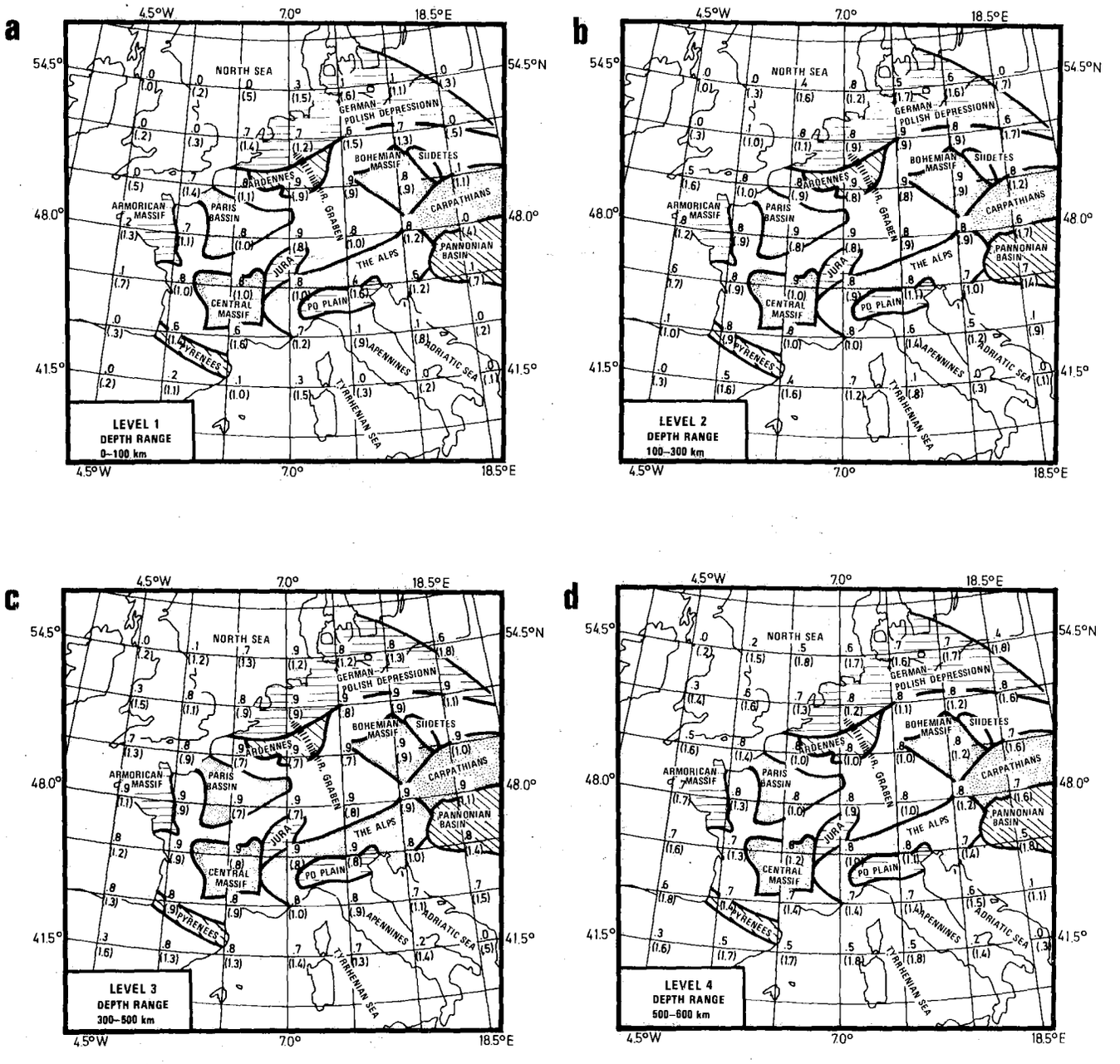

Fig. VI.4.4a Resolution and standard error (in brackets) estimates for all level 1 nodes. Geographical locations referred to in the text are also indicated.

b Resolution and standard error (in brackets) estimates for all level 2 nodes.

c Resolution and standard error (in brackets) estimates for all level 3 nodes.

d Resolution and standard error (in brackets) estimates for all level 4 nodes.

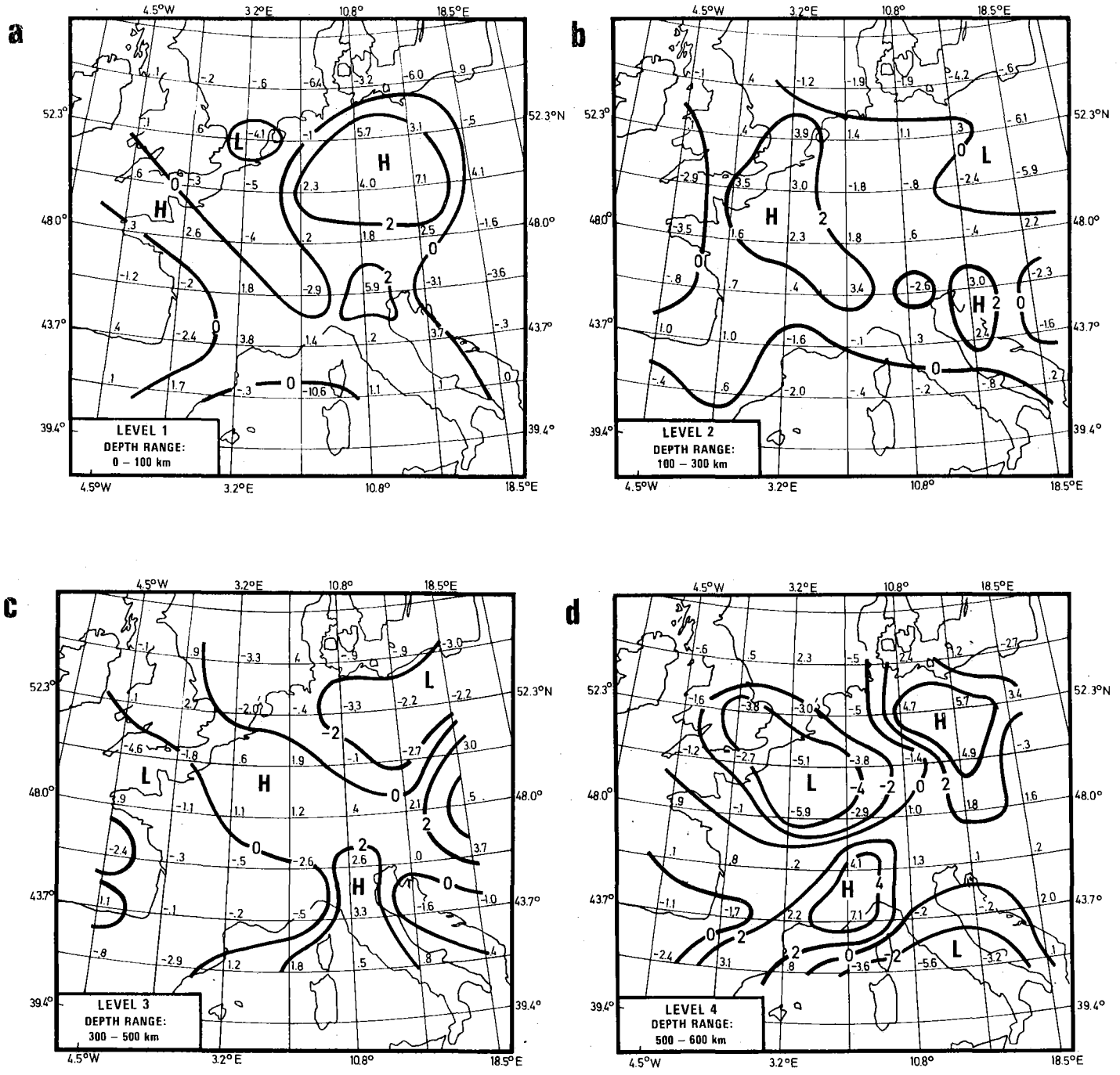

Fig. VI.4.5a Velocity perturbations (in per cent) for level 1. Areas of high and low velocities are indicated by capital letters H and L. Resolution and standard errors for all nodes are displayed in Fig. VI.4.4a.

b Velocity perturbations (in per cent) for level 2. Otherwise as for Fig. VI.4.5a.

c Velocity perturbations (in per cent) for level 3. Otherwise as for Fig. VI.4.5a.

d Velocity perturbations (in per cent) for level 4. Otherwise as for Fig. VI.4.5a.